

Final Report for NAG1-01-012

**Modeling Disturbance Dynamics in
Transitional and Turbulent Boundary Layers**

C.E. Grosch

Old Dominion University, Norfolk, Virginia 23529

Final Report for NAG1-01-012

**Modeling Disturbance Dynamics in
Transitional and Turbulent Boundary Layers**

C.E. Grosch

Old Dominion University, Norfolk, Virginia 23529

Abstract

The dynamics of an ensemble of linear disturbances in boundary-layer flows at various Reynolds numbers is studied through an analysis of the transport equations for the mean disturbance kinetic energy and energy dissipation rate. Effects of adverse and favorable pressure-gradients on the disturbance dynamics are also included in the analysis. Unlike the fully turbulent regime where nonlinear phase scrambling of the fluctuations affects the flow field even in proximity to the wall, the early stage transition regime fluctuations studied here are influenced across the boundary layer by the solid boundary. In addition, the dominating dynamics in the disturbance kinetic energy equation is governed by the energy production, pressure-transport and viscous diffusion – also in contrast to the fully turbulent regime. For the disturbance dissipation rate, a dynamic balance exists between the destruction and diffusion of dissipation.

1 Introduction

A current challenge in the prediction of wall-bounded turbulent flow fields within the realm of single-point closures is the inability to consistently predict the (upstream) flow field natural transition region. While some transition-sensitized turbulence models, applicable to naturally transitioning flows, exist in the literature,[1, 2, 3] their development has been based more on empirical grounds rather than on first principles. As such, their range of applicability is confined to flows containing the same dynamic features as the “calibration flows” the models were designed for. In contrast, transition-sensitized turbulence models, applicable to flows with by-pass transition, have been extensively studied and refined over the last decade (e.g. see Steelant and Dick[4] and Savill[5]).

Motivated by the success of such models in flows with by-pass transition, a methodology is pursued here that can lead to the development of models applicable to generic flows in a natural, low-disturbance environment. These models have immediate use in the prediction of many flow fields including complex aerodynamic flows such as flows over high-lift devices. While transition dynamics and transition models have been and continue to be studied and developed, their applicability is confined to the understanding and prediction of transition. On the other hand RANS-type closure models, for example, are used to predict entire flow fields. From these predictions, lift and drag characteristics of aerodynamic vehicles are obtained for use in design and flow control. Even in simple flows over flat surfaces, current RANS-type turbulence models without modification, can and often do yield results that show “turbulent profiles” in the immediate vicinity of the leading edge even though transition to turbulence occurs much further downstream.

In order to develop a general linkage between the transitioning laminar flow and the turbulent flow in a developing boundary layer, it is necessary to have a common mathematical framework from which the disturbances in both regimes can be described. Previous studies,[6, 7] have developed such a framework by coupling a deterministic description of the evolution of disturbances in the laminar regime with an analysis of an ensemble of such disturbances. The approach is based on the observation that, even in the laminar regime, every flow is subject to an inevitable uncertainty in initial conditions. Therefore, although each individual disturbance evolves deterministically, a probability distribution must be introduced for the calculation of ensemble mean properties of the various disturbance statistical moments.

For the boundary-free homogeneous decaying disturbances[6] and for the homogeneous shear[7] cases studied previously, an arbitrary disturbance mode was characterized by three independent wave numbers, so that the probability distribution P was necessarily a function of (k_1, k_2, k_3) . The isotropy of the initial disturbance field implied that P was a function of k^2 . A Gaussian distribution was chosen by appealing to the central limit theorem: i.e., the ensemble of disturbances contained an infinite number of statistically independent modes. The modes are statistically independent because there are no nonlinear interactions among them, and according to the central limit theorem, the probability density function of a large number of statistically independent entities approaches a Gaussian as the number of entities goes to infinity.

This approach is similar to rapid distortion theory (RDT) in that it is based on linearized disturbance equations; however the development is different in detail. In RDT, the energy spectrum tensor and corresponding transport equations that are developed can include the effects of viscosity and have relied on the homogeneity of the disturbance field. Here, the probability distribution associated with each initial disturbance mode is given and from that a statistical database of such a distribution of disturbances is developed. In the previous studies,[6, 7] the disturbance dynamics focused on homogeneous flows (shear-free flow[6], shear flow[7]) in order to develop the methodology and to form a linkage with corresponding turbulent boundary-free flows. Nevertheless, the process can be extended to inhomogeneous flows as well, at least over some spatial range where the amplitudes of the disturbances remain small relative to the mean flow.

The mathematical methodology developed previously is now extended to a spatially developing boundary layer with zero, adverse and favorable pressure gradients. This study focuses on the earliest stages of transition in a low disturbance environment where the disturbance amplitudes are small enough that nonlinear interactions can be neglected. In this regime the disturbance field typically involves a wide spectrum of Tollmien-Schlichting (TS) modes and streamwise vortices. The streamwise vortices make no contribution to the production of disturbance kinetic energy and for small amplitude disturbances they eventually decay, [8] while the stable TS modes rapidly decay also, leaving a superposition of least stable modes.[9] The (mean) boundary-layer flow is extracted from the Falkner-Skan family of solutions, and the disturbance field consists of linear superpositions of three-dimensional disturbance modes that are solutions of the linearized Navier-Stokes equations. We assume the existence of such a field without enquiring as to its origin. Each disturbance mode is characterized by a frequency, spanwise wavenumber, and a streamwise and spanwise position of origin. For each frequency and spanwise wavenumber, the streamwise wavenumber for the most unstable mode at the particular Reynolds number is selected. With the Reynolds number, frequency, spanwise wavenumber, and streamwise wavenumber fixed, the modal "shape" is determined by the solutions of the equations for the velocity and pressure fields.

The disturbance field consists of modes that could originate anywhere over the boundary. Since the disturbances have no preferred location of origin, the distribution in frequency and spanwise wavenumber space of the disturbance field is assumed to be homogeneous in the streamwise and spanwise directions. A probability distribution that is uniform in frequency and Gaussian in spanwise wavenumber space characterizes such a random disturbance field. The frequency range is sufficiently broad to encompass the most unstable disturbance modes, and the wavenumber range is sufficiently broad that the ensemble contains spatially localized three-dimensional disturbances. While the choice of ensemble is homogeneous, the disturbance modes streamwise wavenumber and "shape" retain a dependence on streamwise location. This implies that the disturbance correlations built from the choice of (homogeneous) ensemble and (inhomogeneous) disturbance modes are also dependent on streamwise location. In order to enforce the homogeneity condition that the same ensemble of disturbances is generated at each streamwise location, the probability distribution also contains a delta function in streamwise

position. This probability distribution is used to compute single-point second moments that characterize the disturbance field as well as its kinetic energy and dissipation rate budgets. It is worth noting that other more complex (inhomogeneous) disturbances, such as those generated by three-dimensional mean flows and cross-flow vortices, could be considered within this current framework. Even in this more complex case, an ensemble of such disturbances would be formed with an associated probability distribution in the same manner as detailed here for the linear disturbance modes. However, in this initial study, the simpler two-dimensional mean flow with pressure gradient effects will suffice in developing this new formulation.

As noted above, current RANS-type closure models have difficulty in representing pre-transition flow fields and transition location, particularly with nonzero pressure gradients or for three dimensional mean flows. Although three dimensional mean flows are not considered here, the effects of zero, favorable, and adverse pressure gradients on the kinetic energy and dissipation rate budgets are considered. The information obtained from these balance equations is needed in order to guide the formulation of a unified model.

2 Wall-Bounded Disturbance Fields

A flat solid-walled boundary located in the (x_1^*, x_3^*) plane at $x_2^* = 0$ is considered (* variables are dimensional quantities). The incompressible flow analysis focuses downstream away from any leading edge effects. Linear disturbance fields are generated which are deviations from an ensemble-mean boundary-layer velocity field given by the Falkner-Skan family of solutions, $U(Re, \beta, x_2)$, applicable to flow fields with zero, adverse and favorable pressure gradients. Standard boundary-layer scaling is used so that U_∞^* is the velocity scale, $L^* = [(2 - \beta) \nu^* x_1^* / U_\infty^*]^{1/2}$ is the length scale, and $Re (= U_\infty^* L^* / \nu^*)$ is the Reynolds number. The effects of pressure gradient are introduced through the parameter β : $\beta = 0$, zero pressure gradient; $\beta < 0$, adverse pressure gradient; $\beta > 0$, favorable pressure gradient.

The three-dimensional, laminar disturbance modes under consideration are bounded solutions of the linearized Navier-Stokes equations. These velocity and pressure disturbance modes can be written as

$$\begin{bmatrix} \hat{u}_i(x_2, k_3, \omega, Re) \\ \hat{p}(x_2, k_3, \omega, Re) \end{bmatrix} e^{i(\int_{x_{10}}^{x_1} k_1 dx'_1 + k_3(x_3 - x_{30}) - \omega t)} \quad (1)$$

where $(k_1(Re, \omega, k_3), 0, k_3)$ is the wave vector in coordinate directions (x_1, x_2, x_3) associated with the most unstable mode, (k_1 complex and k_3 real), ω is the (real) frequency, and (x_{10}, x_{30}) is the position where the disturbance mode originates. Note that the disturbance mode shapes \hat{u}_i and \hat{p} depend on streamwise position through their Reynolds number dependence. Since k_3 is independent of position, the phase $e^{-ik_3 x_{30}}$ can be absorbed into \hat{u}_i and \hat{p} . In the analysis that follows, it will also be convenient to analyze the results in terms of the displacement thickness Reynolds number $Re_\theta (= U_\infty^* \theta^* / \nu^*)$ where the displacement thickness is given by $\theta^* = L^* \int_0^\infty U(1 - U) dx_2$.

These modes are the solutions of the continuity and momentum equations given by

$$ik_1 \hat{u}_1 + \frac{d\hat{u}_2}{dx_2} + ik_3 \hat{u}_3 = 0 \quad (2)$$

$$(-i\omega + ik_1 U) \hat{u}_1 + \left(\frac{dU}{dx_2} \right) \hat{u}_2 = -ik_1 \hat{p} + \frac{1}{Re} [\mathcal{L}\hat{u}_1] \quad (3)$$

$$(-i\omega + ik_1 U) \hat{u}_2 = -\frac{d\hat{p}}{dx_2} + \frac{1}{Re} [\mathcal{L}\hat{u}_2] \quad (4)$$

$$(-i\omega + ik_1 U) \hat{u}_3 = -ik_3 \hat{p} + \frac{1}{Re} [\mathcal{L}\hat{u}_3] \quad (5)$$

with

$$\mathcal{L} = \frac{d^2}{dx_2^2} - (k_1^2 + k_3^2) = \frac{d^2}{dx_2^2} - \mathcal{K}^2 \quad (6)$$

where $U(Re, x_2)$ is the mean (streamwise) velocity. As seen from Eqs. 2 – 5, it is assumed throughout that \hat{u}_i , \hat{p} , and k_1 are only weakly dependent on x_1 so that their derivatives with respect to x_1 can be neglected. These equations are combined to obtain, first the Orr-Sommerfeld equation for the wall normal velocity component \hat{u}_2 with complex eigenvalue k_1

$$\mathcal{L}^2 \hat{u}_2 = iRe(k_1 U - \omega) \mathcal{L}\hat{u}_2 - ik_1 Re \left(\frac{d^2 U}{dx_2^2} \right) \hat{u}_2 \quad (7)$$

and second, the Squire equation for the normal component of vorticity,

$$\hat{\zeta}_2 = ik_3 \hat{u}_1 - ik_1 \hat{u}_3. \quad (8)$$

$$\frac{d^2 \hat{\zeta}_2}{dx_2^2} + [iRe(\omega - k_1 U) - \mathcal{K}^2] \hat{\zeta}_2 = ik_3 Re \left(\frac{dU}{dx_2} \right) \hat{u}_2 \quad (9)$$

Equations (7) and (9) are solved subject to the boundary conditions $\hat{u}_2 = (d\hat{u}_2/dx_2) = 0$, $\hat{\zeta}_2 = 0$ at $x_2 = 0$, and $\hat{u}_2 \rightarrow 0$, $\hat{\zeta}_2 \rightarrow 0$ as $y \rightarrow \infty$. Equation (7) is solved using the compound matrix algorithm employing a fourth order Runge-Kutta integration combined with an iteration on the eigenvalue. Once the eigenvalue, k_1 , and eigenfunction, \hat{u}_2 , are found, Eq. (9) can be solved for $\hat{\zeta}_2$. This equation is quite stiff so it is solved by an implicit method; the second derivative is approximated by a fourth order stencil and the resulting penta-diagonal system is solved by a generalized Thomas algorithm. With \hat{u}_2 and $\hat{\zeta}_2$ known, Eqs. (2) and (8) are solved simultaneously for \hat{u}_1 and \hat{u}_3 . Finally, with the velocity $\hat{\mathbf{u}}$ known, the pressure is found from (3).

The velocity and pressure disturbance fields can be constructed from these disturbance mode solutions by considering an ensemble of linear superpositions of modes with initial mode amplitudes $\Phi(\omega, k_3, x_{10})$ so that

$$u_i(\mathbf{x}, t) = \int d\omega dk_3 dx_{10} \Phi(\omega, k_3, x_{10}) \hat{u}_i(x_2, \omega, k_3, Re) e^{i(\int_{x_{10}}^{x_1} k_1 dx'_1 + k_3 x_3 - \omega t)} \quad (10)$$

$$p(\mathbf{x}, t) = \int d\omega dk_3 dx_{10} \Phi(\omega, k_3, x_{10}) \hat{p}(x_2, \omega, k_3, Re) e^{i(\int_{x_{10}}^x k_1 dx'_1 + k_3 x_3 - \omega t)} \quad (11)$$

This ensemble is described by a probability distribution for the amplitudes so that their mean, $\langle \Phi(\omega, k_3, x_{10}) \rangle$ is zero, and covariance is homogeneous (x_1 and x_3 -directions) and stationary.

$$\langle \Phi^*(\omega, k_3, x_{10}) \Phi(\omega', k'_3, x_{10}) \rangle = \delta(\omega - \omega') \delta(k_3 - k'_3) \delta(x_{10} - x'_{10}) P(\omega, k_3, x_{10}). \quad (12)$$

Assuming that ω , k_3 , and x_{10} are independent random variables, the probability density $P(\omega, k_3, x_{10})$ is partitioned as

$$P(\omega, k_3, x_{10}) = P_\omega(\omega) P_{k_3}(k_3) P_{x_{10}}(x_{10}) \quad (13)$$

The distribution in ω cannot be Gaussian because ω does not take negative values. Negative ω 's, which correspond to upstream propagating modes, are all heavily damped. If a Gaussian distribution in ω was taken with positive mean, this would introduce a preferred frequency. The probability density $P_\omega(\omega)$ is therefore assumed to be that of band limited white noise having a flat spectrum and a corresponding probability distribution,

$$P_\omega(\omega) = \begin{cases} \frac{1}{\omega_H - \omega_L} & \omega_L < \omega < \omega_H \\ 0 & \text{otherwise} \end{cases} \quad (14)$$

where ω_L and ω_H are chosen to encompass the region of disturbance growth computed from linear stability theory. As discussed in the Introduction, for each frequency and spanwise wavenumber, the streamwise wavenumber for the most unstable mode at the particular Reynolds number is selected. Figure 1 shows the growth rate contours obtained from the linear stability analysis for the zero pressure gradient case as a function of ω and Re_θ for different values of k_3 . The frequency range used must be large enough to encompass both growing and decaying modes over the corresponding k_3 and Reynolds number ranges. In the calculations, ω was chosen to lie in the range 0.04 to 0.08 with the step in ω between these limits being 0.001. For the zero pressure gradient case, it can be seen from Figure 1 that, for the range of k_3 values shown in the figure, the lower frequency modes will be damped at the smaller values of Re_θ and the higher frequency modes will be damped at the larger values of Re_θ . The results reported here are relatively insensitive to the range of values of ω provided that it is not too narrow.

For $P_{k_3}(k_3)$, the central limit theorem argues in favor of a Gaussian and such a Gaussian distribution should have a large variance in order to encompass a sufficient wavenumber range of energetic oblique modes. The disturbances should be localized in the spanwise direction so this is a further argument for a relatively large variance. Therefore the probability density $P_{k_3}(k_3)$ assumes a Gaussian form

$$P_{k_3}(k_3) = \frac{1}{\sqrt{2\pi\sigma^2}} \exp\left(-\frac{k_3^2}{2\sigma^2}\right) \quad (15)$$

with variance σ^2 , corresponding to a mean spanwise, spatial extent of the disturbances given by σ^{-1} . The results were found not to vary when a sufficiently large variance in k_3 was used. For example, results were essentially unchanged for values of $\sigma \geq 0.1$ that corresponded to a spanwise, spatial extent of the disturbances of $6\theta^*$ and less. For this study, the k_3 values ranged from -0.3 to 0.3 with a step size of 0.001. This range was sufficiently broad so that the values of $P_{k_3}(k_3)$ at the ends of the range were small.

As discussed at the outset, it is not possible to uniquely identify a position of origin for the disturbance field. Thus, a homogeneous ensemble of disturbances is considered and its dynamic behavior at various streamwise locations is examined. Since the mean velocity in the boundary layer is inhomogeneous in the streamwise direction, the probability distribution must also depend on the streamwise position of the origin of the disturbance x_{10} . Thus, a probability density function $P_{x_{10}}$ is needed that generates the same ensemble of disturbances at each streamwise location x_1 . Such a distribution is given by

$$P_{x_{10}}(x_{10}) = \delta(x_1 - x_{10}) \quad (16)$$

This wall-bounded disturbance field contrasts with the homogeneous fields[6, 7] studied previously. In this case an ensemble of superpositions of most unstable modes is considered rather than an ensemble of superpositions of all modes that was considered in the homogeneous case. For a given (ω, k_3) , there is a unique k_1 corresponding to the most unstable mode, so the probability distribution depends on ω and k_3 but not k_1 .

In further contrast to the homogeneous cases considered previously,[6, 7] where the evolution of the disturbance correlations was studied, in this inhomogeneous case the same ensemble is created at each x_1 and the instantaneous dynamical behavior of the disturbance correlations is studied. If the boundary-layer disturbance field were allowed to evolve, the differential growth or decay rates of the modes would lead to a rapid loss of streamwise homogeneity introducing an arbitrary element into the analysis. It is, therefore, more useful to consider an instantaneous snapshot of the dynamics.

Based on experimental results with the zero pressure gradient flat plate boundary layer,[10] transition would begin between $Re_x \approx 5 \times 10^5$ to 6×10^5 and end between $Re_x \approx 3 \times 10^6$ and 10^7 . In terms of Re_θ , the beginning of transition would occur between 470 and 515 while the end would occur between 1150 and 2100. The calculations in this study cover the range $150 \leq Re_\theta \leq 2000$ which should encompass the transition range.

3 Disturbance Velocity Correlations and Dissipation Rate

It is now possible to form the second-moment correlations from the disturbance velocity and pressure fields given in Eqs. (10) and (11). For example, the disturbance stress tensor is given by

$$\begin{aligned} \tau_{ij}(x_1, x_2) &= \frac{1}{2} \left\langle u_i^* u_j + u_i u_j^* \right\rangle \\ &= \frac{1}{2} \int d\omega dk_3 P_\omega(\omega) P_{k_3}(k_3) \left(\hat{u}_i^* \hat{u}_j + \hat{u}_i \hat{u}_j^* \right), \end{aligned} \quad (17)$$

with the disturbance kinetic energy, $K = \tau_{ii}/2$, and the disturbance isotropic dissipation rate is given by

$$\varepsilon(x_1, x_2) = \frac{1}{Re} \left\langle \frac{\partial u_j}{\partial x_k} \frac{\partial u_j^*}{\partial x_k} \right\rangle$$

$$\begin{aligned}
&= \frac{1}{Re} \int d\omega dk_3 P_\omega(\omega) P_{k_3}(k_3) \\
&\quad \times \left[(|k_1|^2 + k_3^2) \hat{u}_j^* \hat{u}_j + \frac{d\hat{u}_j^*}{dx_2} \frac{d\hat{u}_j}{dx_2} \right]
\end{aligned} \tag{18}$$

Note that, although streamwise homogeneity in the choice of ensemble has been maintained, all disturbance correlations retain a dependence on x_1 through either a direct Reynolds number dependence (as in the disturbance dissipation rate) or through the implicit Reynolds number dependence of \hat{u}_i and k_1 . From these quantities, it is now possible to construct a detailed mapping of the ensemble-averaged disturbance field.

The necessarily low-Reynolds numbers of interest here suggest that the various disturbance correlations be analyzed in terms of wall units. The friction velocity u_τ^* needed in the scaling is determined from $\sqrt{\tau_w^*}$, where the wall shear stress τ_w^* is simply proportional to dU^*/dx_2^* at $x_2^* = 0$ with $U^*(x_2)$ obtained from the solution of the Falkner-Skan equation with pressure gradient parameter β ,

$$u_\tau^2 = \left(\frac{u_\tau^*}{U_\infty^*} \right)^2 = \left(\frac{\nu^*}{U_\infty^* L^*} \right) \left(\frac{dU}{dx_2} \right)_{x_2=0} = \left(\frac{S_0}{Re} \right). \tag{19}$$

The corresponding scaled wall normal coordinate x_2^+ is then,

$$x_2^+ = \left(\frac{x_2^* u_\tau^*}{\nu^*} \right) = \left(\frac{x_2^*}{L^*} \right) \left(\frac{U_\infty^* L^*}{\nu^*} \right) \left(\frac{S_0}{Re} \right)^{1/2} = (S_0 Re)^{1/2} x_2, \tag{20}$$

where both S_0 and Re are functions of β . (All the variables to be presented in the figures to follow are scaled and shown in wall units.) In order to compare results at different values of Re_θ , the kinetic energy of the disturbance field at each Re_θ is normalized to unity. This normalization determines the overall scaling of all other quantities.

Before examining the disturbance energy and dissipation rate budgets, the different components of the disturbance stress tensor are discussed. Disturbance ensembles at two different Re_θ values are chosen. The first is $Re_\theta = 393$, which corresponds to a region just downstream of the neutral position; here the disturbances contain both components that grow and decay but DK/Dt is negative. The second value is $Re_\theta = 1040$, which characterizes a region where almost all disturbance components are growing and DK/Dt is positive.

Figure 2 shows the behavior of the disturbance normal stress components across the boundary layer. The τ_{11} and τ_{33} components both reach peak values near $x_2^+ \approx 25$. At $Re_\theta = 1040$, Figure 2b, the distributions of all three components are broader in x_2^+ than at $Re_\theta = 393$, Figure 2a. The peak value of both τ_{11} and τ_{22} are also both slightly greater at $Re_\theta = 1040$ than at $Re_\theta = 393$ but the peak value of τ_{33} is slightly less. An interesting contrast to the fully turbulent case, even at these low-Reynolds numbers,[11] is the behavior of the τ_{22} and τ_{33} components. Unlike the turbulent case where $\tau_{22} > \tau_{33}$ in the inner part of the layer, the behavior here is just the opposite with $\tau_{33} > \tau_{22}$. The streamwise τ_{11} component still dominates these other two

components over the inner part of the boundary layer. The τ_{22} component continues to increase away from the wall and eventually decays at a slower rate than either the τ_{11} or τ_{33} components, and becomes the dominant component in the outer part of the boundary layer.

The shear stress distribution at four values of Re_θ , 149, 393, 627 and 1040, is shown in Figure 3. The production of kinetic energy is proportional to $-\tau_{12}$ so that a negative τ_{12} means that the the transfer of energy is from the mean flow to the disturbance field while a positive τ_{12} means that the transfer of energy is from the disturbance field to the mean flow. The location at which $Re_\theta = 149$ is upstream of the neutral location, all components of the disturbance field are decaying at this position and the shear stress is positive across the entire boundary layer. At $Re_\theta = 393$ the shear stress is negative in the near wall region and positive in the outer region of the boundary layer, being predominantly positive. A further increase in Re_θ to 647 results in an increase in the size of the region where τ_{12} is negative; here the disturbance field is a mixture of growing and decaying modes and $DK/Dt \approx 0$ throughout the boundary layer. At $Re_\theta = 1040$ the shear stress is negative across the entire boundary layer and DK/Dt is positive. This change in the distribution of τ_{12} with increasing Re_θ mirrors the change from a region where all of the disturbance components are decaying to one in which almost all of them are growing. The distribution of τ_{12} with x_2^+ at $Re_\theta = 1040$ is typical of the larger Reynolds numbers. Calculations were performed up to values of $Re_\theta \approx 2000$. Over the range $1000 \leq Re_\theta \leq 2000$, the peak negative value of τ_{12} and its x_2^+ location changed by much less than 1%. Increasing Re_θ from 1000 to 2000 only results in a very slow widening of the long ‘tail’ in the outer portion of the boundary layer; at $Re_\theta \approx 1800$ it extends to $x_2^+ \approx 150$ in contrast to $x_2^+ \approx 110$ at $Re_\theta = 1040$. The low Reynolds number results cannot be used for RANS modeling but were included in order to illustrate the effects of varying the Reynolds number. As these results show, the shear stress varies with Reynolds number up to $Re_\theta \approx 1000$ and is relatively insensitive to further increase in Re_θ .

With the Falkner-Skan family of solutions it is straightforward to introduce the effect of pressure gradient into the analysis through the variation of the parameter β . Calculations have been performed for three values of β : 0.00, -0.15 , and 0.15 . As discussed previously, the first of these, $\beta = 0.00$, yields the zero pressure gradient Blasius mean flow profile. With $\beta = -0.15$, the boundary layer faces a moderately strong adverse pressure gradient (the separating Falkner-Skan flow occurs for $\beta = -0.198840$); the mean flow wall shear stress is approximately 46% of that of the zero pressure gradient boundary layer. Finally, $\beta = 0.15$ produces a moderately strong favorable pressure gradient with the mean flow wall shear stress about 40% greater than that of the zero pressure gradient boundary layer. Thus, the three values of β span a reasonable range of mean flows.

Figure 4 shows the effect of imposing an adverse ($\beta < 0$) or favorable ($\beta > 0$) pressure gradient at $Re_\theta \approx 1040$; Figure 4a is a plot of K versus x_2 Figure 4b is a plot of K versus x_2^+ . In the three cases shown, the total disturbance energy within the boundary layer is normalized to unity. The adverse pressure gradient thickens the boundary layer which is reflected in the broadening of the kinetic energy distribution relative to the zero pressure gradient ($\beta = 0$) case. A local minimum in the distribution now exists at $x_2^+ \approx 30$ and this corresponds to the inflection

point in the the mean velocity profile caused by the adverse gradient. In contrast, the favorable pressure gradient causes a thinning of the boundary layer which is reflected in the movement of the peak of the kinetic energy distribution closer to the solid boundary at $x_2^+ \approx 20$.

The effect of pressure gradient on disturbance dissipation rate is shown in Figure 5. Unlike the kinetic energy, the dissipation rate is essentially unaffected by the change in pressure gradient. The dissipation rate peaks at the boundary and is confined to a very narrow region near the solid boundary with the maximum value at the boundary only slightly affected by the change in β .

In the fully turbulent case, it is not uncommon to exploit energetic equilibrium (production equals dissipation) conditions that exist across the boundary layer. For example, in the log-layer region, the production-to-destruction equilibrium can be used as a rationale for a Boussinesq eddy viscosity relation between the turbulent shear stress and mean velocity gradient. While such a production-to-destruction balance is unlikely to occur in this linear disturbance region, it is nevertheless of interest to see if a similar eddy viscosity relation can be established here. Figure 6 shows the behavior of $-\tau_{12}/(dU/dx_2^+)$ across the boundary layer as a function of pressure gradient. For the zero pressure gradient case, this disturbance mode viscosity increases with distance from the wall and peaks near $x_2^+ = 25$ – consistent with the distributions of the other disturbance quantities. In an adverse pressure gradient, the disturbance mode viscosity level increases with the peak moving farther away from the solid boundary. Nevertheless, in both cases the distributions near the wall ($x_2^+ \leq 10$) nearly coincide. The favorable pressure gradient case is not shown here since $DK/Dt < 0$ and the shear stress (production) is positive (negative) (cf. Figure 7).

The ensemble of disturbances described in the previous section must also satisfy a dynamic balance derivable from the linear Navier-Stokes equations. The dynamics of the disturbance field can be better understood through an analysis of the balance equations derivable for the disturbance kinetic energy and dissipation rate.

3.1 Disturbance energy budget

The derivation of the transport equations for the disturbance kinetic energy, $K = \tau_{ii}/2$, follows directly from the linearized Navier-Stokes equations coupled with an average over an ensemble of disturbances described by the distribution $P(\omega, k_3, x_{10})$. The resulting transport equation can be written as

$$\frac{DK}{Dt} = \mathcal{P} - \varepsilon + \Pi + \mathcal{D} \quad (21)$$

where

$$\mathcal{P} = -\tau_{12} \frac{dU}{dx_2} \quad (22)$$

$$\Pi = -\frac{1}{2} \frac{\partial}{\partial x_j} \langle u_j^* p + u_j p^* \rangle \quad (23)$$

$$\mathcal{D} = \frac{1}{Re} \frac{\partial^2 K}{\partial x_j \partial x_j} \quad (24)$$

are, respectively, the disturbance energy production, pressure-transport of disturbance energy, and viscous diffusion of disturbance energy. The disturbance energy dissipation rate is ε given in Eq. (18). Note that in the subsequent figures, DK/Dt is not a streamwise difference but is computed as an instantaneous quantity according to an expression analogous to Eqs. (17) and (18).

Using this disturbance energy equation, it is instructive to examine the behavior of the disturbance ensemble at different streamwise locations. At low Re_θ (not shown) where there are no growing modes in the ensemble, the disturbance kinetic energy decays ($DK/Dt < 0$) because production, the contribution from dissipation and viscous diffusion are all negative. Only pressure-transport contributes positively to the energetic balance over most of the layer. Very near the wall, the dynamic balance is between the kinetic energy dissipation rate and viscous diffusion, which is analogous to the fully turbulent case very near the wall.

Figure 7 shows the energy budget across the boundary layer at the two different values of Re_θ . At each value of Re_θ , the distributions of energy production, dissipation rate, pressure-transport, and viscous diffusion are shown. Figure 7a shows the energy balance at $Re_\theta = 393$; a region of the flow where some unstable modes are included in the ensemble. At this value of Re_θ , there exists regions of the boundary layer where, for example, production is positive and pressure-transport is negative although overall $DK/Dt < 0$. Very near the wall the balance is predominantly between viscous diffusion and disturbance dissipation rate. Figure 7b shows the energy balance at $Re_\theta = 1040$. At larger values of Re_θ , the qualitative features of the energetic balance remain unchanged with only the tails of each distribution decaying more slowly with x_2^+ reflecting the downstream boundary-layer growth. At this and larger values of Re_θ , the kinetic energy is growing with $DK/Dt > 0$ across the boundary layer. Again, the near wall balance is between viscous diffusion and disturbance dissipation rate. It is apparent from Figure 7b that, outside of the very near-wall region, the production and pressure transport have opposite sign and are nearly proportional to one another although viscous diffusion also contributes to the balance. It is possible to show (see Appendix) that this proportionality between the pressure-transport and energy production can be established through an analysis of the Poisson equation for the pressure fluctuations.

The effect of imposed pressure gradient on the disturbance kinetic energy budget is shown in Figure 8 at $Re_\theta \approx 1040$. In the adverse pressure gradient case ($\beta < 0$), Figure 8a, the dynamic balance between the terms in the transport equation remain unchanged; however, there is a broadening of the distribution across the layer and an overall increase in the amplitude levels associated with each term except the disturbance dissipation rate. Note that the scale in Figure 8a is five times that in Figure 7b and Figure 8b. For the favorable pressure gradient case shown in Figure 7b, the dynamic balance is significantly altered qualitatively from the zero pressure gradient case. The dynamic balance is more consistent with the $Re_\theta = 393$ zero pressure gradient case shown in Figure 7a. At this streamwise station, the ensemble of disturbances included both stable and unstable modes, but the overall balance showed a decay of disturbance kinetic energy

across the boundary layer.

These results confirm that even though the individual disturbance modes satisfy the linear Navier-Stokes equations, an ensemble of such disturbances can display a complex range of energetic dynamics which characterize the early stage transition regime of a developing flow. In the next section, the dynamic balance of the disturbance dissipation rate is examined.

3.2 Disturbance dissipation rate budget

The transport equation for the disturbance dissipation rate ε is also directly derivable from the linearized momentum equations. The resulting form is given by

$$\frac{D\varepsilon}{Dt} = \underbrace{\mathcal{P}_\varepsilon^1 + \mathcal{P}_\varepsilon^2 + \mathcal{P}_\varepsilon^3}_{\mathcal{P}_\varepsilon} - \Upsilon + \Pi_\varepsilon + \mathcal{D}_\varepsilon \quad (25)$$

where

$$\mathcal{P}_\varepsilon^1 = -\frac{1}{Re} \frac{dU}{dx_2} \left\langle \frac{\partial u_1^*}{\partial x_j} \frac{\partial u_2}{\partial x_j} + \frac{\partial u_1}{\partial x_j} \frac{\partial u_2^*}{\partial x_j} \right\rangle \quad (26)$$

$$\mathcal{P}_\varepsilon^2 = -\frac{1}{Re} \frac{dU}{dx_2} \left\langle \frac{\partial u_j^*}{\partial x_1} \frac{\partial u_j}{\partial x_2} + \frac{\partial u_j}{\partial x_1} \frac{\partial u_j^*}{\partial x_2} \right\rangle \quad (27)$$

$$\mathcal{P}_\varepsilon^3 = -\frac{1}{Re} \frac{d^2 U}{dx_2^2} \left\langle u_2^* \frac{\partial u_1}{\partial x_2} + u_2 \frac{\partial u_1^*}{\partial x_2} \right\rangle \quad (28)$$

$$\Upsilon = \frac{2}{Re^2} \left\langle \frac{\partial^2 u_j^*}{\partial x_k \partial x_r} \frac{\partial^2 u_j}{\partial x_k \partial x_r} \right\rangle \quad (29)$$

$$\Pi_\varepsilon = -\frac{1}{Re} \frac{\partial}{\partial x_j} \left\langle \frac{\partial u_j^*}{\partial x_k} \frac{\partial p}{\partial x_k} + \frac{\partial u_j}{\partial x_k} \frac{\partial p^*}{\partial x_k} \right\rangle \quad (30)$$

$$\mathcal{D}_\varepsilon = \frac{1}{Re} \frac{\partial^2 \varepsilon}{\partial x_i \partial x_i} \quad (31)$$

are, respectively, mixed production, production by mean velocity gradient, gradient production, destruction, pressure-transport, and viscous diffusion. (The notation used here is consistent with the notation used by Rodi and Mansour.[13]) Analogous to the treatment of the DK/Dt term, $D\varepsilon/Dt$ is not a streamwise difference but is computed as an instantaneous quantity.

Figure 9 shows the balance of terms across the boundary layer for the disturbance dissipation rate budget. With the exception of the destruction and viscous diffusion of dissipation, which essentially balance out across the entire boundary layer, all terms are negligible. This behavior suggests that in the absence of a production mechanism associated with vortex stretching, a nonlinear effect, direct dissipation of disturbance energy is confined to regions in close proximity to the wall. In contrast with the disturbance energy balances, the same (qualitative) dynamic balance is achieved for the two values of Re_θ shown and was also found for all values of Re_θ

at which these calculations were carried out ($Re_\theta \leq 2000$) The only change that was found was the broadening of the distribution across the layer with increasing Re_θ . While energetic equilibrium ($DK/Dt = 0$) only occurred at a single value of Re_θ , Figure 9 shows that $D\varepsilon/Dt$ is very small and ≈ 0 compared to the dominant terms, destruction and viscous diffusion of dissipation, throughout the entire range of Re_θ values studied. In fact, it was found that $D\varepsilon/Dt$ was always at least three orders of magnitude smaller than the dominant terms.

The effect of pressure gradient on the disturbance dissipation rate balance is shown in Figure 10. Unlike the disturbance energy balances shown in Figures 7 and 8, the dissipation rate dynamics is insensitive to the imposition of pressure gradient on the flow. This once again shows that the disturbance dissipation rate is not a (significant) contributor to the disturbance dynamics in the early stage transition regime.

4 Conclusions

The dynamics of an ensemble of disturbances in boundary-layer flow with and without pressure gradient has been studied. The individual disturbance modes are solutions of the linearized Navier-Stokes equations and the probability density function associated with the ensemble accounts for distributions in spanwise wavenumber, frequency and initial spatial position. Such an ensemble represents the early stages of a transition disturbance field which ultimately leads to a fully turbulent field. The representation used here has been shown in previous homogeneous studies[6, 7] to form a unified mathematical framework between the two fields.

An analysis of the dynamic balance in the disturbance kinetic energy and dissipation rate equations has shown behavior which contrasts with the fully turbulent case at both low Reynolds numbers and in near-wall regions. This new insight is critical in properly representing the dynamics in the linear disturbance region. While no self-similar behavior is reached, the qualitative features of the dynamic balance become independent of Re_θ and show that energy production, pressure-transport, and viscous diffusion dominate across the boundary layer with a small contribution from dissipation rate. The dissipation rate only plays a role in very close proximity to the solid boundary where it balances the energy diffusion.

The dynamics of the disturbance dissipation rate transport are straightforward. In the absence of nonlinear interactions, there is essentially no production mechanism present so that all the dissipation rate originates at the solid boundary. The disturbance field dissipation rate is unaltered in the region ($D\varepsilon/Dt = 0$) because a dynamic balance between the dominant terms, destruction and diffusion, is achieved across the boundary layer.

The results obtained here provide new insight into the dynamic balance of an ensemble of disturbances in the early stages of a (naturally) transitioning boundary-layer flow in a low disturbance environment. Since current RANS-type closure models are not capable of predicting transition region location without modification, the information here can be used to develop improved transport equations for the ensemble of disturbances and subsequently coupled to corresponding transport equations valid in the fully turbulent regime..

Relationship Between Disturbance Energy Production and Pressure Transport

From the results presented in Sec. 3.1 and Figure 9, it was shown that a close relationship exists between the production of disturbance energy and pressure-transport of disturbance energy. In this appendix, the relationship will be derived and the proportionality coefficient between the two terms estimated.

From Eqs. (17) and (22), the production of disturbance energy can be written as

$$\mathcal{P} = -\frac{1}{2} \langle u_1^* u_2 + u_1 u_2^* \rangle \frac{dU}{dx_2} \quad (32)$$

and the pressure-transport Π is defined by Eq. (23).

In the linear regime, the pressure Poisson equation is given by

$$\nabla^2 p = -2 \frac{\partial u_j}{\partial x_i} \frac{\partial U_i}{\partial x_j} = -2 \frac{\partial u_2}{\partial x_1} \frac{dU}{dx_2}, \quad (33)$$

with solution

$$p(\mathbf{x}) = -2 \int d^3 \mathbf{x}' G(\mathbf{x} - \mathbf{x}') \frac{\partial u_2}{\partial x'_1} \frac{dU}{dx'_2} - \int_S dS \left[G(\mathbf{x} - \mathbf{x}') \frac{\partial p(\mathbf{x}')}{\partial n'} - p(\mathbf{x}') \frac{\partial G(\mathbf{x} - \mathbf{x}')}{\partial n'} \right]. \quad (34)$$

where G is the Green's function. The surface term in Eq. (34) does not contribute to Π since $u_i = 0$ on the no-slip boundary and at infinity.

In the development of turbulent closure models for higher-order correlations involving the fluctuating pressure,[12] it is assumed that all second derivatives of the mean velocity are small relative to the mean velocity gradient. This same assumption is invoked here so that Eq. (34) can be approximated by

$$p(\mathbf{x}) \approx -2 \frac{dU}{dx_2} \int d^3 \mathbf{x}' G(\mathbf{x} - \mathbf{x}') \frac{\partial u_2}{\partial x'_1} = -2 \frac{dU}{dx_2} \int d^3 \mathbf{x}' \frac{\partial G(\mathbf{x} - \mathbf{x}')}{\partial x_1} u_2(\mathbf{x}') \quad (35)$$

With this expression, the pressure-transport term can be written as

$$\begin{aligned} \Pi(\mathbf{x}) \approx & \left\langle u_j^*(\mathbf{x}) \frac{\partial}{\partial x_j} \left(\frac{dU}{dx_2} \int d^3 \mathbf{x}' \frac{\partial G(\mathbf{x} - \mathbf{x}')}{\partial x_1} u_2(\mathbf{x}') \right) \right. \\ & \left. + u_j(\mathbf{x}) \frac{\partial}{\partial x_j} \left(\frac{dU}{dx_2} \int d^3 \mathbf{x}' \frac{\partial G(\mathbf{x} - \mathbf{x}')}{\partial x_1} u_2^*(\mathbf{x}') \right) \right\rangle \end{aligned} \quad (36)$$

For $j \neq 1$, $\partial^2 G(\mathbf{x} - \mathbf{x}') / \partial x_j \partial x_1$ is odd in x'_1 while u_2 is a slowly varying function of x'_1 . This implies that the integrals in (36) vanish. For $j = 1$, Eq. (36) can be written as

$$\begin{aligned} \Pi(\mathbf{x}) \approx & \frac{dU}{dx_2} \left\langle u_1^*(\mathbf{x}) \left(\int d^3 \mathbf{x}' \frac{\partial^2 G(\mathbf{x} - \mathbf{x}')}{\partial x_1^2} u_2(\mathbf{x}') \right) \right. \\ & \left. + u_1(\mathbf{x}) \left(\int d^3 \mathbf{x}' \frac{\partial^2 G(\mathbf{x} - \mathbf{x}')}{\partial x_1^2} u_2^*(\mathbf{x}') \right) \right\rangle. \end{aligned} \quad (37)$$

The free-space Green's function $-(4\pi |\mathbf{x} - \mathbf{x}'|)^{-1}$ is used so that

$$\frac{\partial^2}{\partial x_j \partial x_j} G(\mathbf{x} - \mathbf{x}') = \delta^3(\mathbf{x} - \mathbf{x}'), \quad (38)$$

and from symmetry this yields

$$\frac{\partial^2}{\partial x_1^2} G(\mathbf{x} - \mathbf{x}') = \frac{\delta^3(\mathbf{x} - \mathbf{x}')}{3}. \quad (39)$$

This allows Eq. (37) to be written as

$$\begin{aligned} \Pi(\mathbf{x}) &\approx \frac{1}{3} \frac{dU}{dx_2} \left\langle u_1^*(\mathbf{x}) \left(\int d^3 \mathbf{x}' \delta^3(\mathbf{x} - \mathbf{x}') u_2(\mathbf{x}') \right) + u_1(\mathbf{x}) \left(\int d^3 \mathbf{x}' \delta^3(\mathbf{x} - \mathbf{x}') u_2^*(\mathbf{x}') \right) \right\rangle \\ &= \frac{1}{3} \frac{dU}{dx_2} \langle u_1^*(\mathbf{x}) u_2(\mathbf{x}) + u_1(\mathbf{x}) u_2^*(\mathbf{x}) \rangle = -\frac{2}{3} \mathcal{P} \end{aligned} \quad (40)$$

From the results shown in Figure 7d, for example, the integrated ratio across the boundary layer between the production and pressure-transport of disturbance energy is ≈ -1 which is in close agreement with the result obtained in Eq. (40). The difference can be easily attributed to the assumption of neglecting the second derivative of the mean velocity in Eq. (35). For example, in the zero pressure gradient case at $x_2^+ = 25$ with $Re_\theta = 1040$, the second derivative of the mean velocity is about one-quarter of the first derivative (in magnitude). Further out in the boundary layer, the second derivative becomes somewhat larger than the first derivative (in magnitude).

References

- [1] J. R. Cho and M. K. Chung, “A k - ϵ - γ equation turbulence model,” J. Fluid Mech. **237**, 301 (1992).
- [2] Y. B. Suzen and P. G. Huang, “Modeling of flow transition using an intermittency transport equation,” ASME J. Fluid Eng. **122**, 273 (2000).
- [3] E. S. Warren and H. A. Hassan, “Transition Closure Model for Predicting Transition Onset,” J. Aircraft **35**, 769 (1998).
- [4] J. Steelant and E. Dick, “Modelling of bypass transition with conditioned Navier-Stokes equations coupled to an intermittency transport equation,” Int. J. Num. Meth. Fluids **23**, 193 (1996).
- [5] A. M. Savill, “By-pass transition using conventional closures,” In: Closure Strategies for Modelling Turbulent and Transitional Flows (B. E. Launder and N. D. Sandham, eds.), Cambridge University Press, Cambridge, 2001.
- [6] W. D. Thacker, T. B. Gatski and C. E. Grosch, “Analyzing Mean Transport Equations of Turbulence and Linear Disturbances in Decaying Flows,” Phys. Fluids **11**, 2626 (1999).
- [7] W. D. Thacker, C. E. Grosch and T. B. Gatski, “Modeling the Dynamics of Ensemble-Averaged Linear Disturbances in Homogeneous Shear Flow,” Flow Turbul. Combust. **63**, 39 (1999).
- [8] H. Salwen and C. E. Grosch, “The Continuous Spectrum of the Orr-Sommerfeld Equation Part 2. Eigenfunction Expansions”, J. Fluid Mech. **104**, 445 (1981). In the example given in Section 6. of this reference, set $U_1 = 0$ and replace x by x_3 and y by x_2 to obtain a periodic (in x_3) array of streamwise vortices. Because any mode is assumed to be uncorrelated with all other modes, only the τ_{12} arising from a mode’s self interaction contributes to the production of kinetic energy. Note that the streamwise vortex modes have $u_1 = 0$ so that their contribution to τ_{12} is identically zero.
- [9] J. Cohen, K. S. Breuer, and J. H. Haritonidis, “On the Evolution of a Wave Packet in a Laminar Boundary Layer,” J. Fluid Mech. **225**, 575 (1991).
- [10] H. Schlichting and K. Gersten, *Boundary-Layer Theory* (8th ed. Springer, Berlin, 2000).
- [11] P. R. Spalart, “Direct simulation of a turbulent boundary layer up to $Re_\theta = 1410$. J. Fluid Mech. **187**, 61 (1988).
- [12] P. Y. Chou, “On Velocity Correlations and the Solutions for the Equations of Turbulent Fluctuation,” Quart. Appl. Math. **3**, 38 (1945).
- [13] W. Rodi and N. N. Mansour, “Low Reynolds number $k - \epsilon$ modelling with the aid of direct simulation data,” J. Fluid Mech. **250**, 509 (1993).

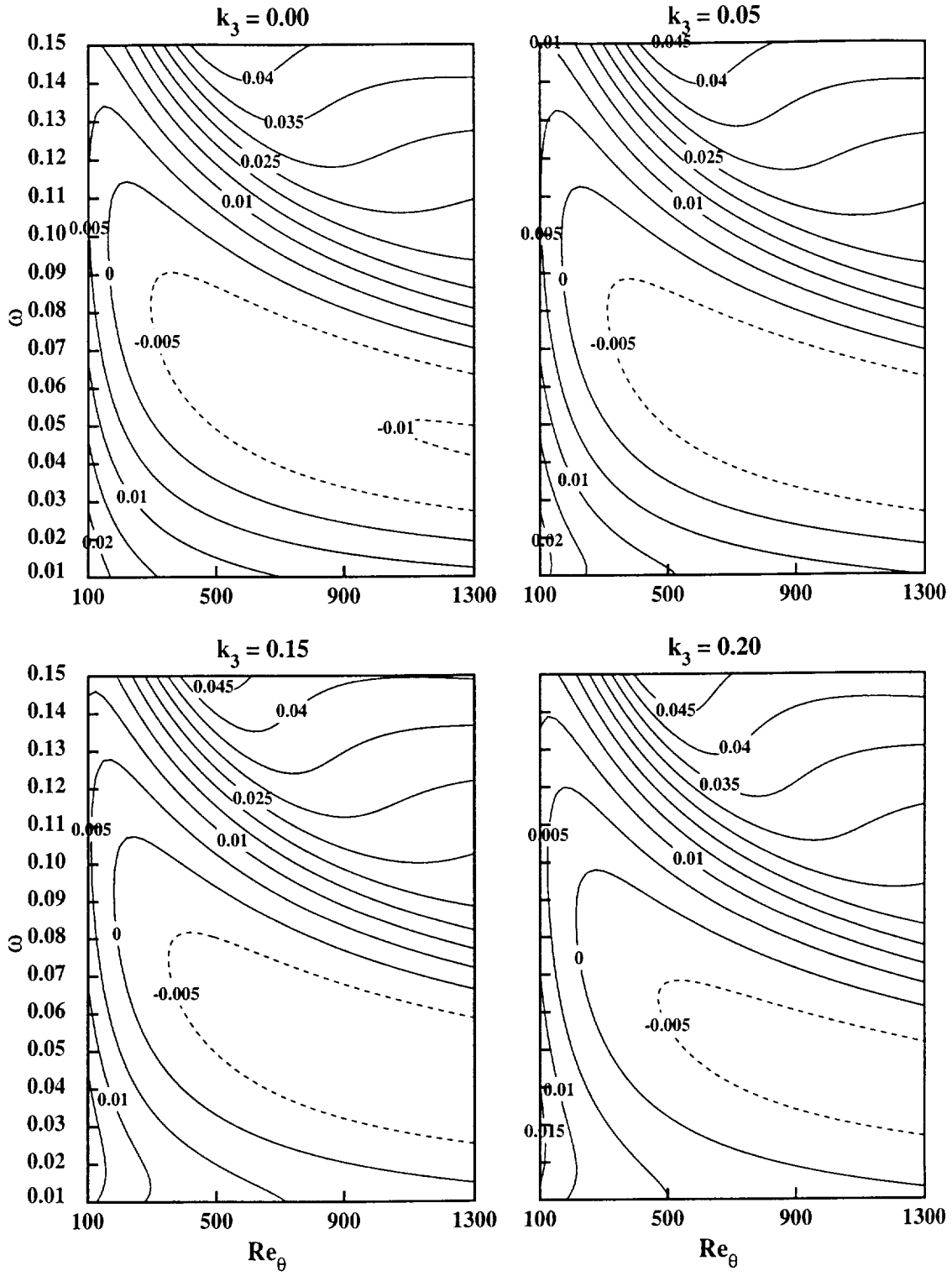


Figure 1: Zero pressure gradient growth-rate contours

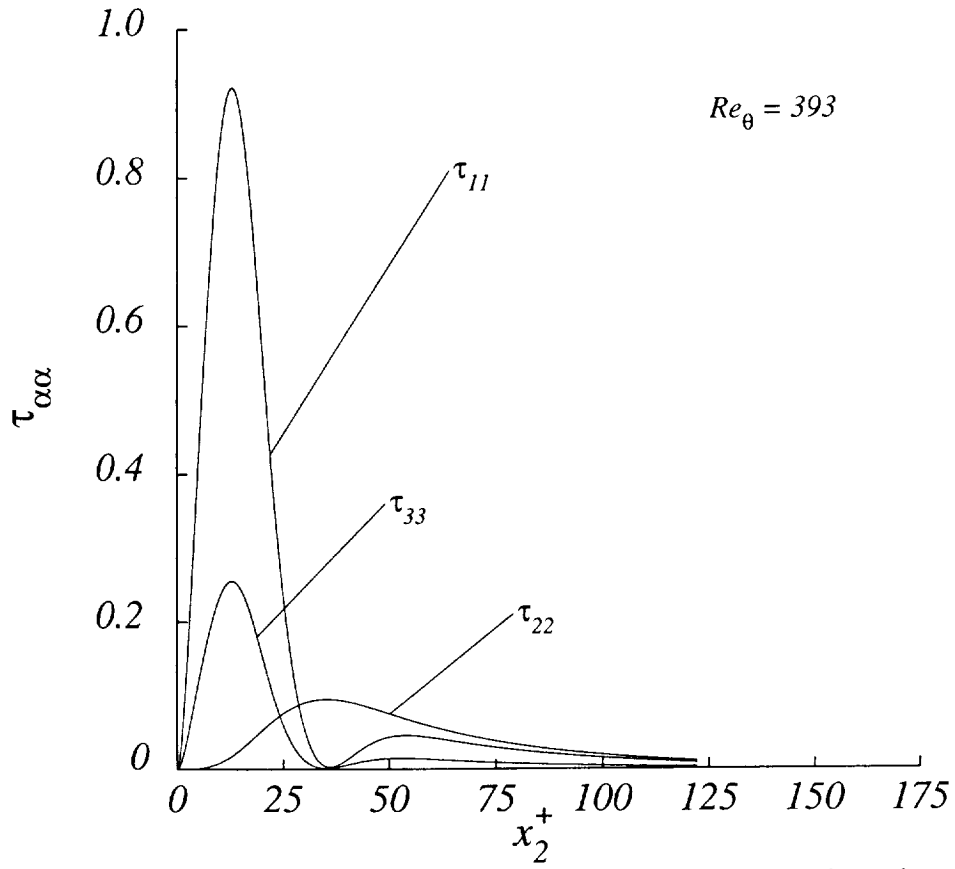


Figure 2a: Variation of disturbance normal stress components across boundary layer (zero pressure gradient) at $Re_\theta = 393$.

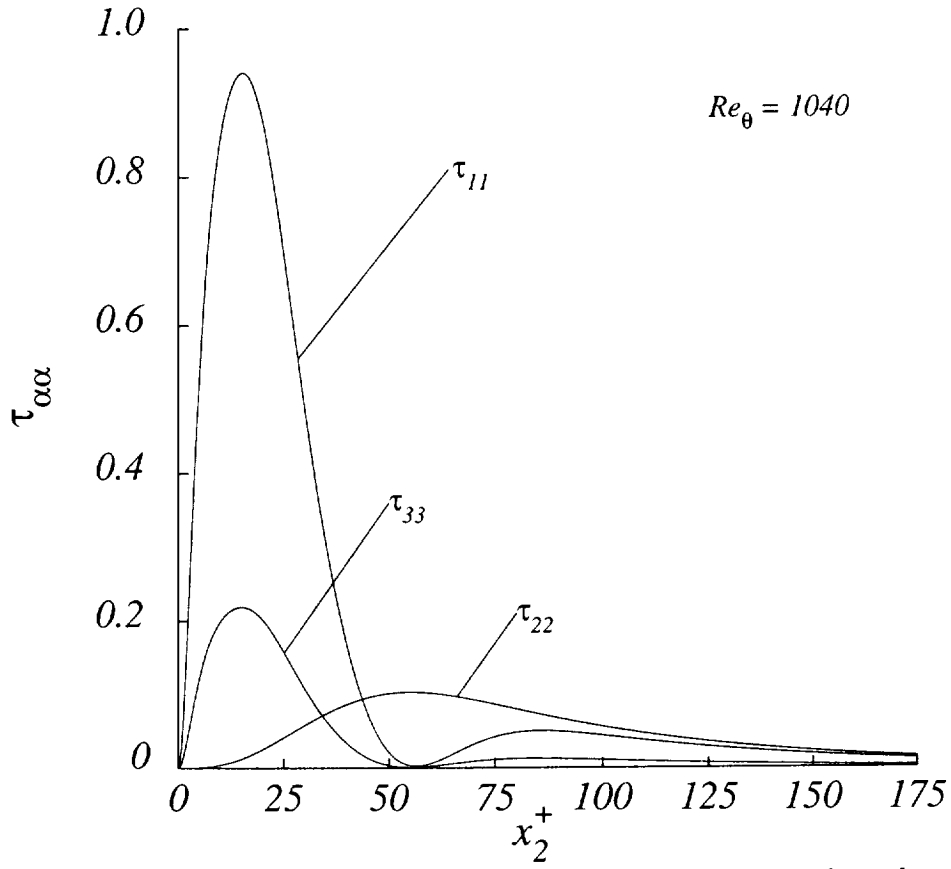


Figure 2b: Variation of disturbance normal stress components across boundary layer (zero pressure gradient) at $Re_\theta = 1040$.

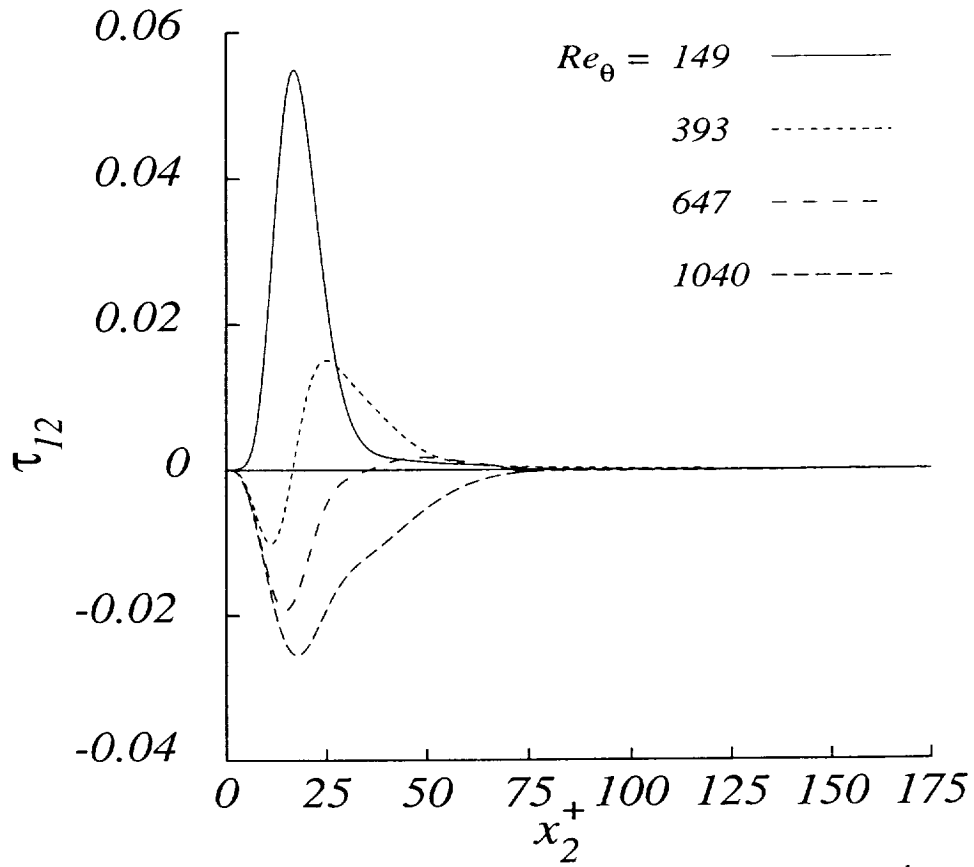


Figure 3: Variation of disturbance shear stress component τ_{12} across boundary layer (zero pressure gradient) at different values of Re_θ .

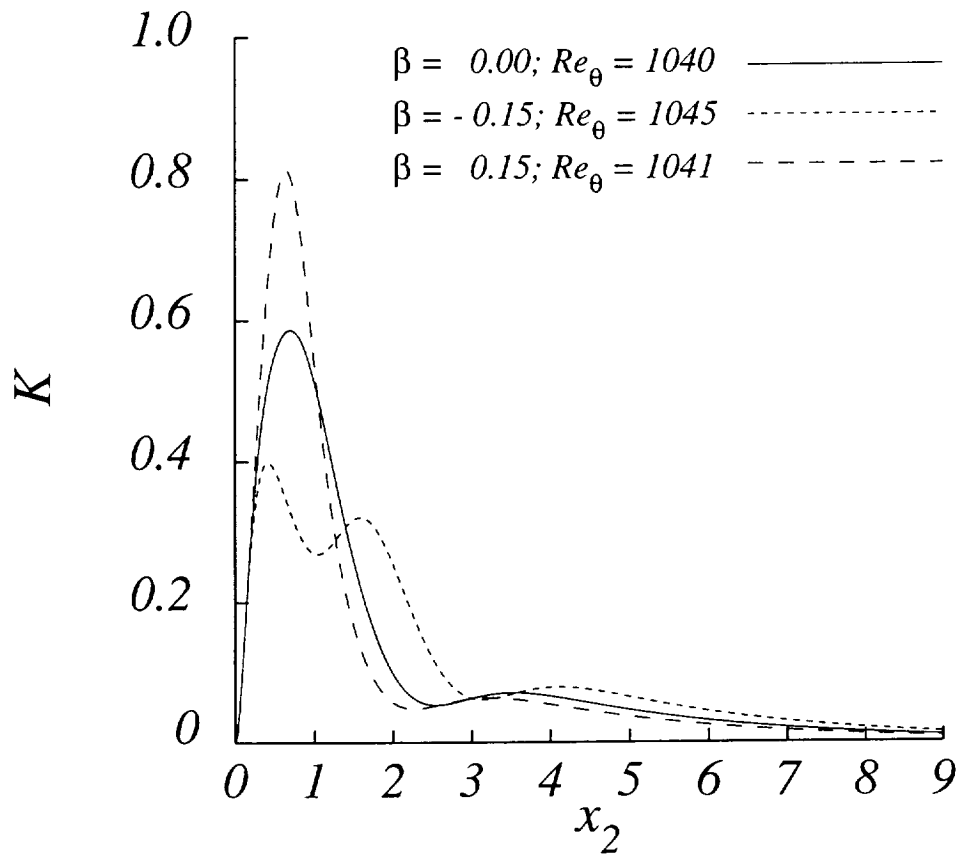


Figure 4a: Effect of pressure gradient on distribution of disturbance kinetic energy.

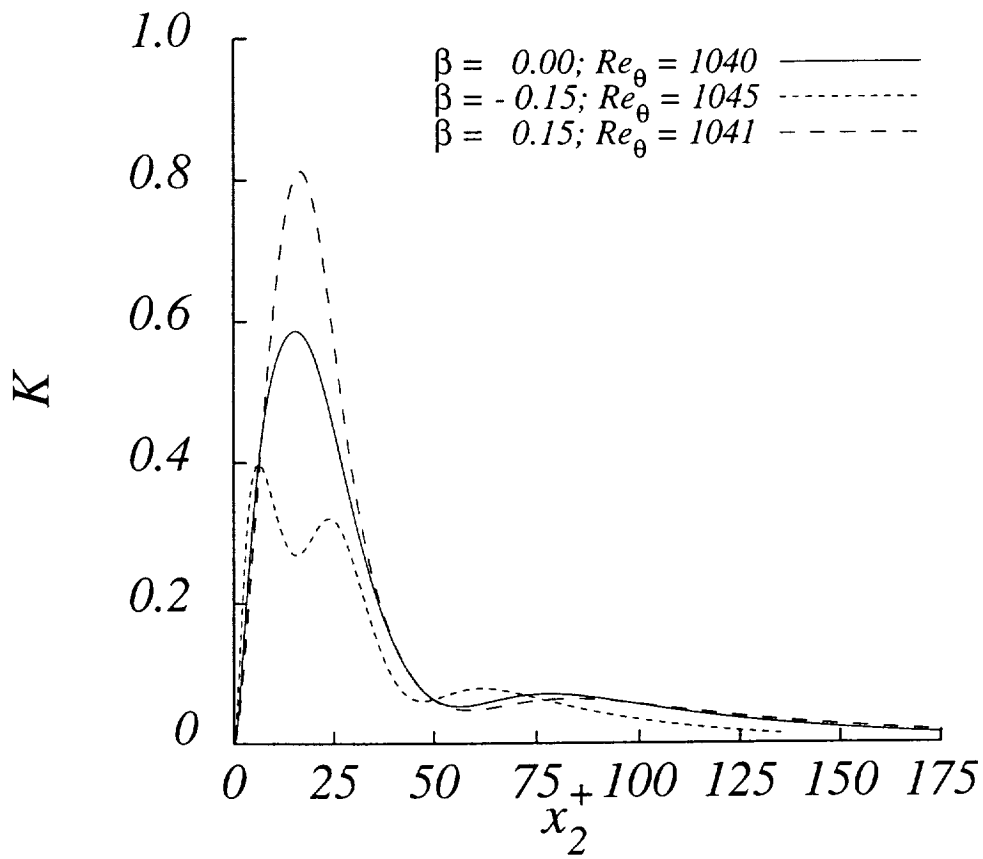


Figure 4b: Effect of pressure gradient on distribution of disturbance kinetic energy.

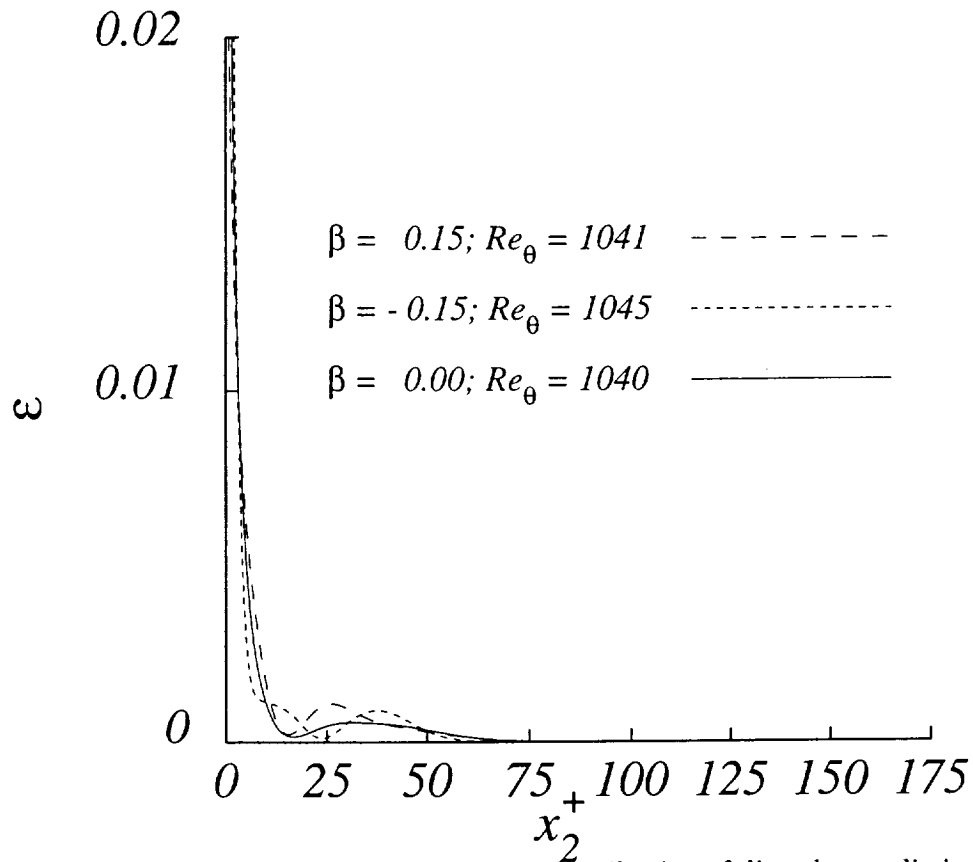


Figure 5: Effect of pressure gradient on distribution of disturbance dissipation rate.

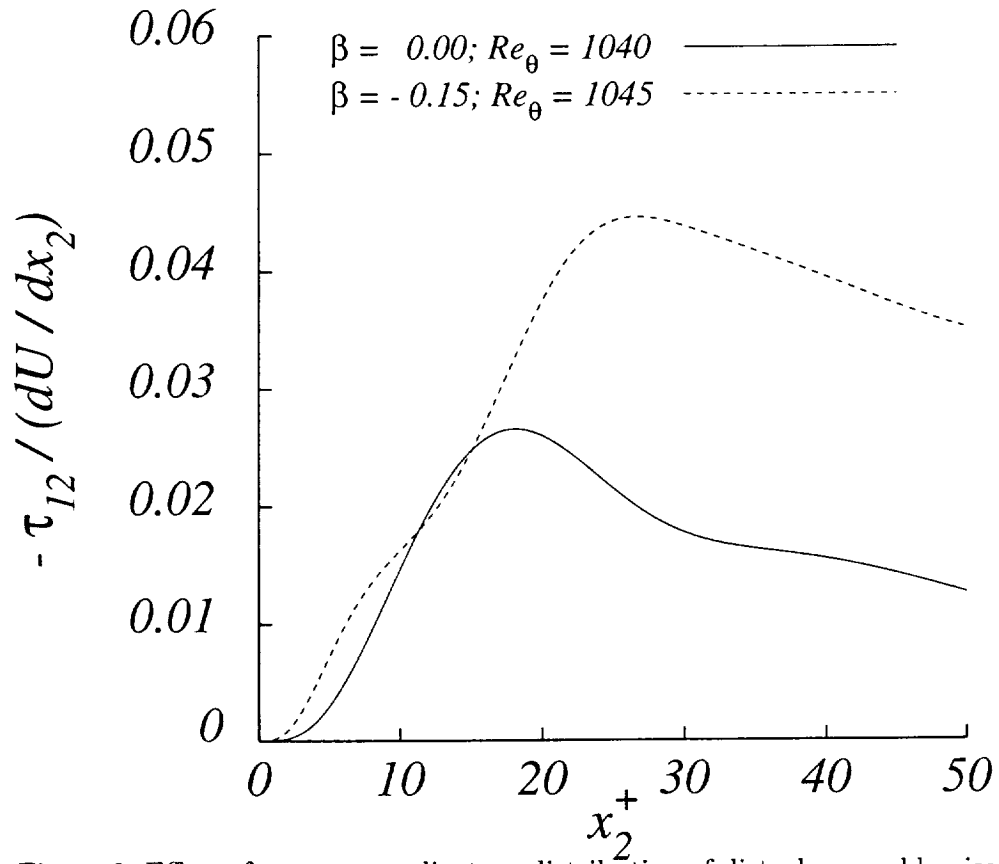


Figure 6: Effect of pressure gradient on distribution of disturbance eddy viscosity.

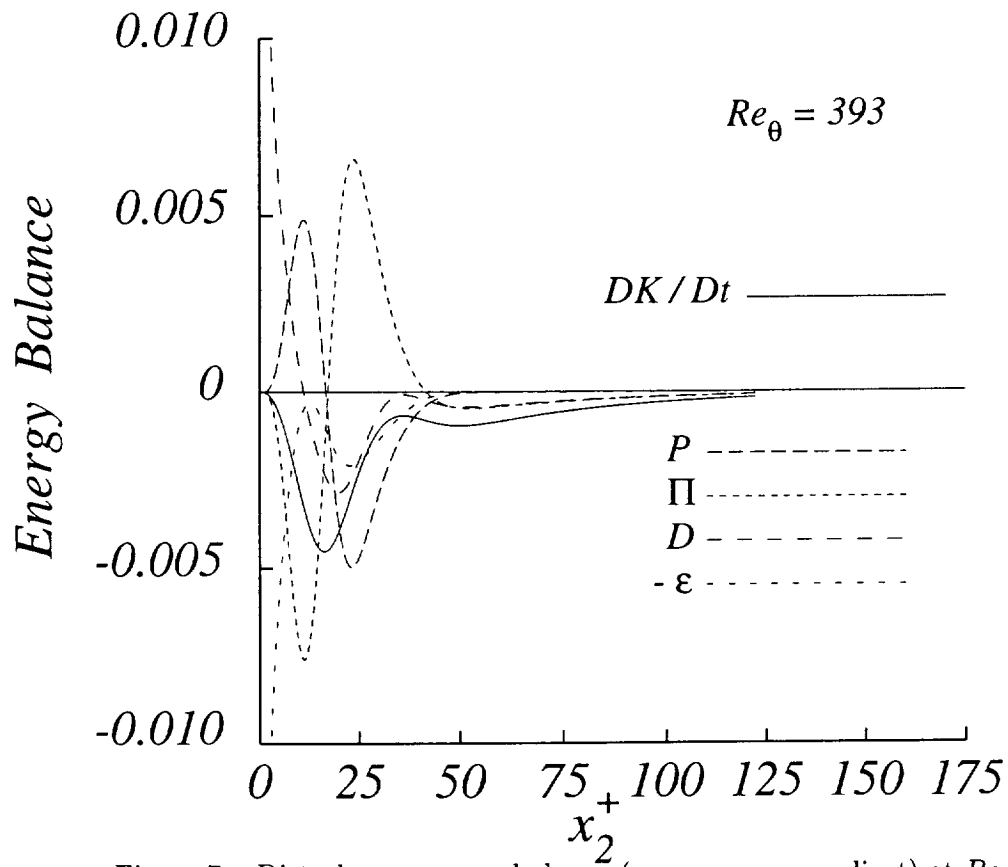


Figure 7a: Disturbance energy balance (zero pressure gradient) at $Re_\theta = 393$.

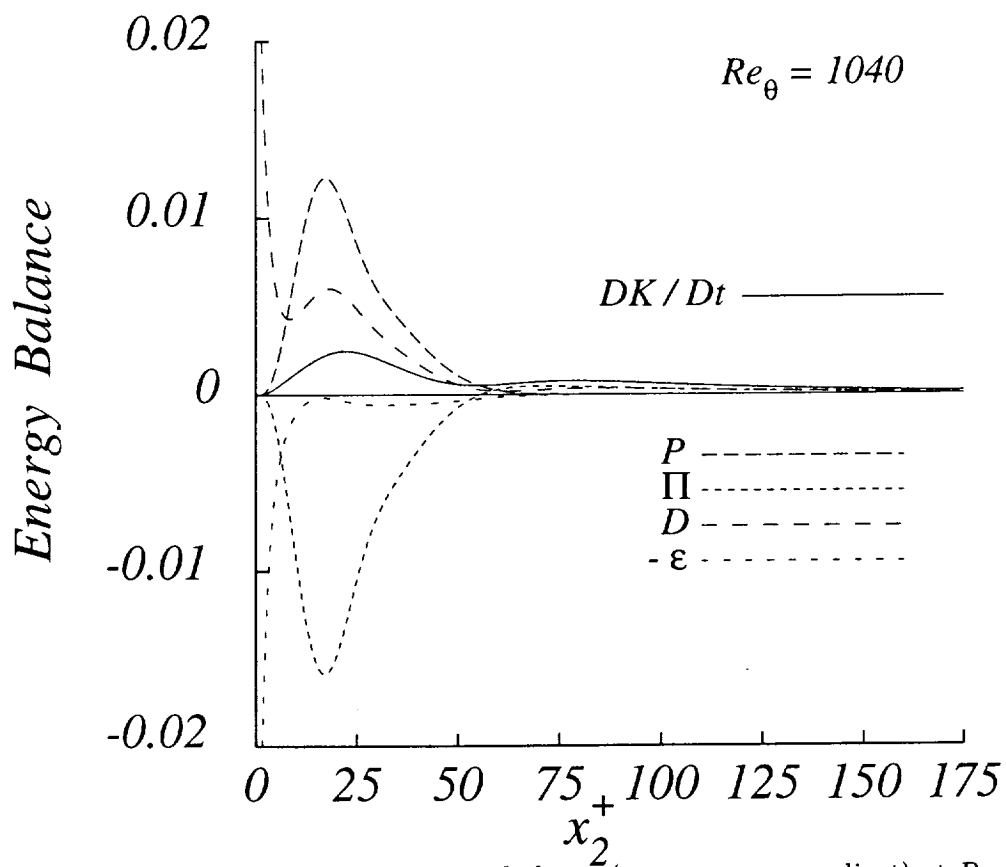


Figure 7b: Disturbance energy balance (zero pressure gradient) at $Re_\theta = 1040$.

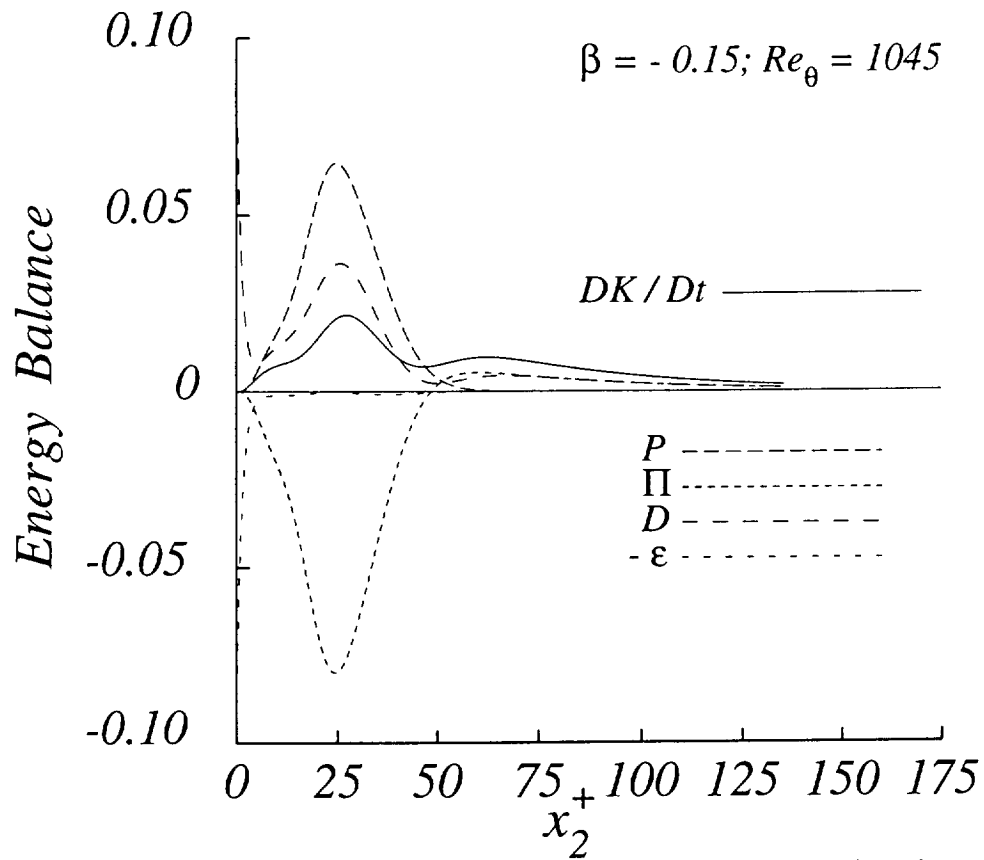


Figure 8a: Effect of an adverse pressure gradient on disturbance kinetic energy balance.

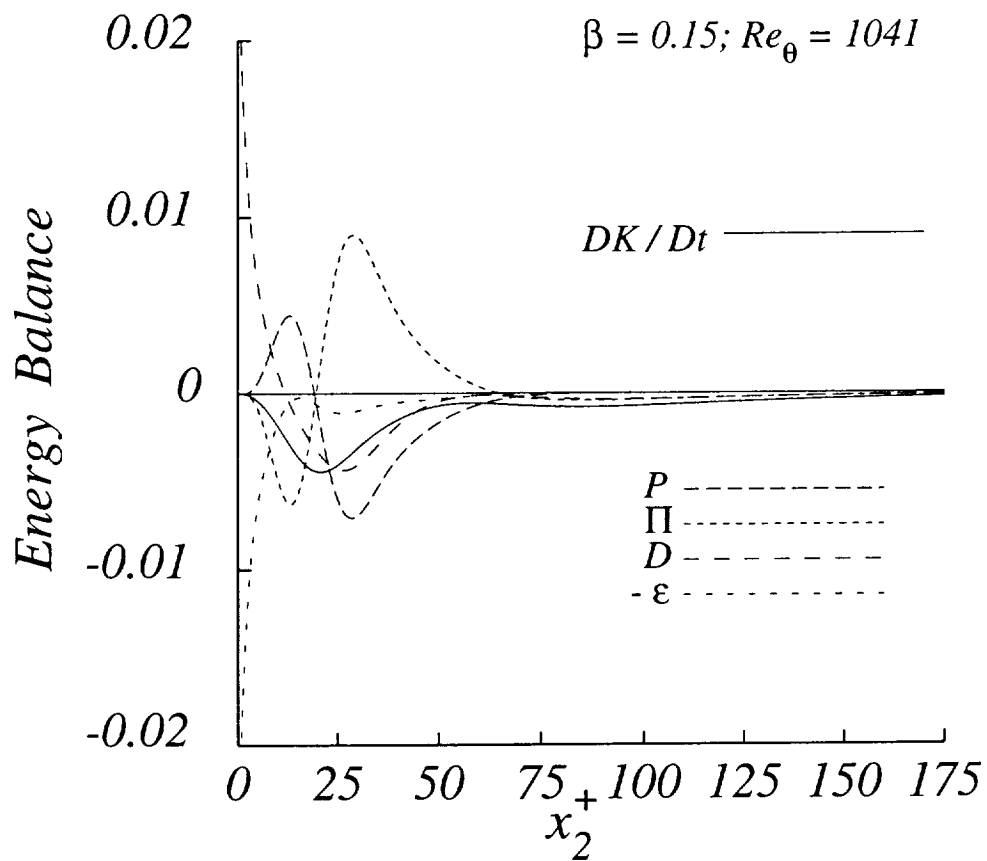


Figure 8b: Effect of a favorable pressure gradient on disturbance kinetic energy balance.

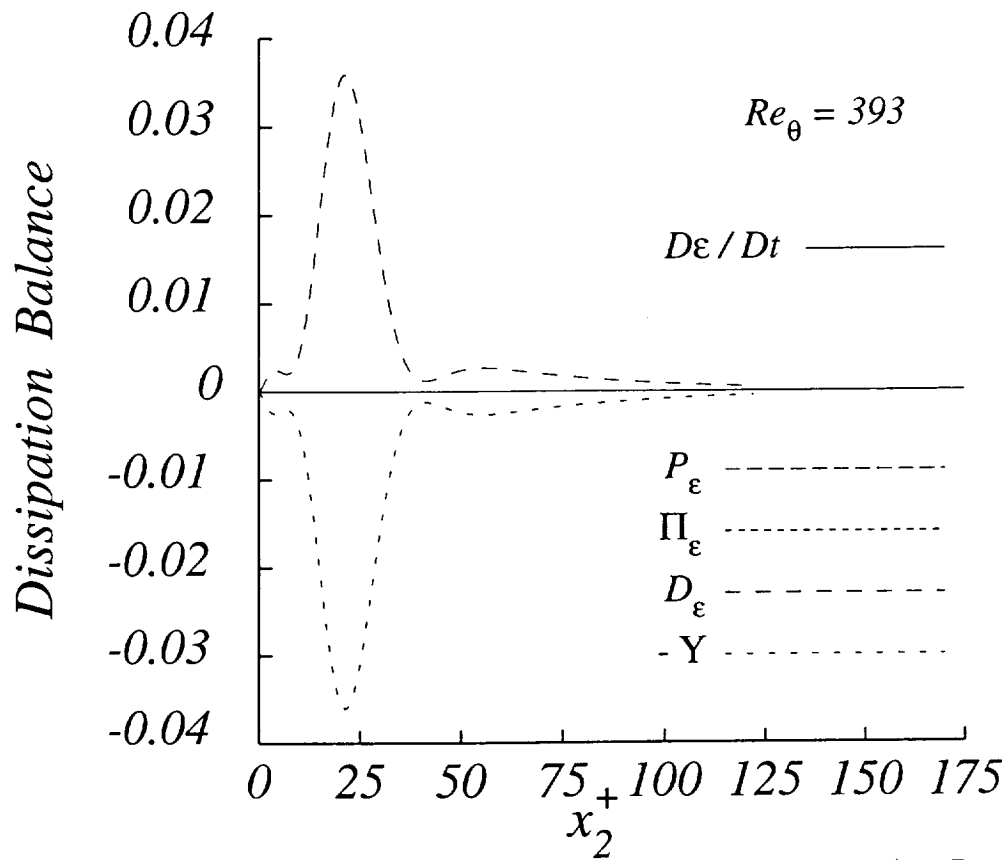


Figure 9a: Disturbance dissipation rate balance (zero pressure gradient) at $Re_\theta = 393$.

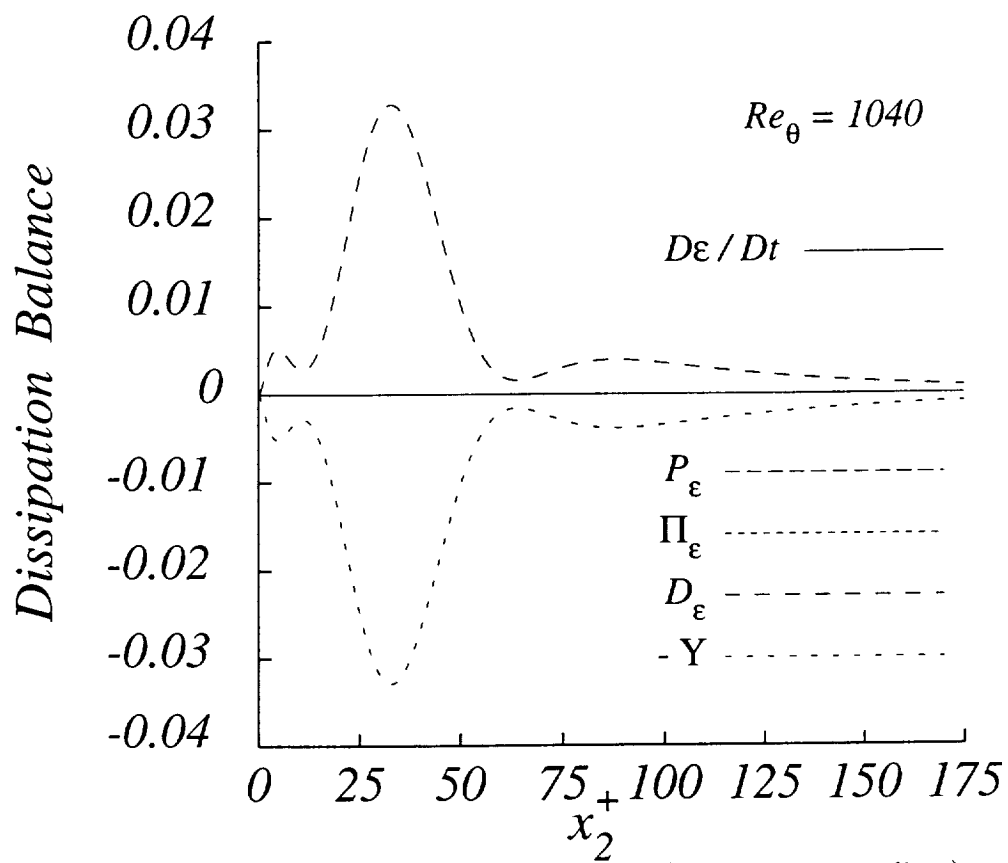


Figure 9b: Disturbance dissipation rate balance (zero pressure gradient) at $Re_\theta = 1040$.

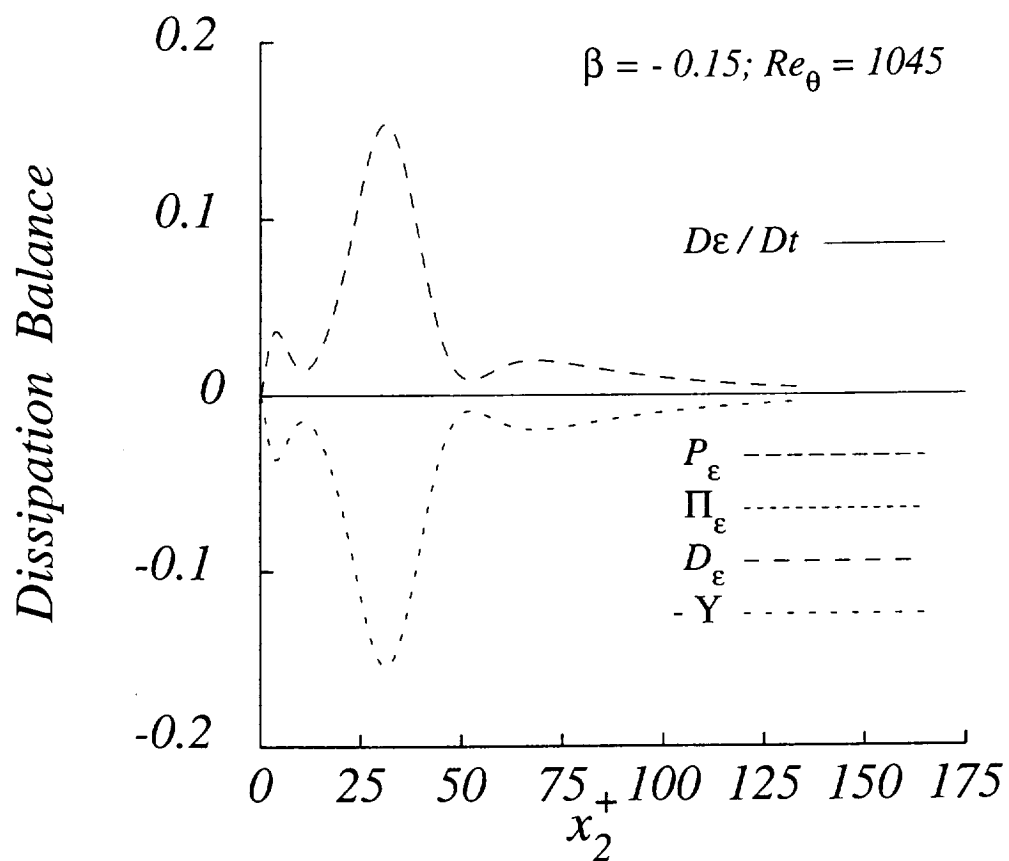


Figure 10a: Effect of an adverse pressure gradient on disturbance dissipating rate balance.

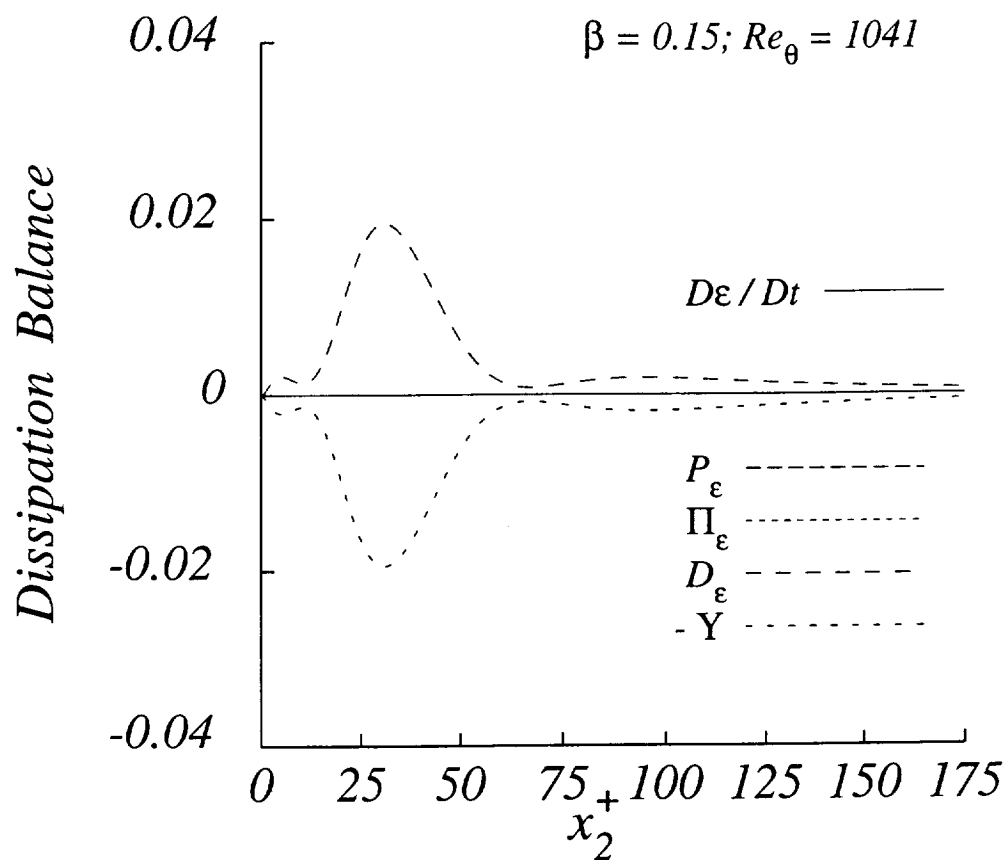


Figure 10b: Effect of a favorable pressure gradient on disturbance dissipating rate balance.

